

# Traceable stitching interferometry for form measurement of moderately curved freeform surfaces

Jan Spichtinger,<sup>a,\*</sup> Michael Schulz,<sup>a</sup> Gerd Ehret<sup>ORCID</sup>,<sup>a</sup> and Rainer Tutsch<sup>b</sup>

<sup>a</sup>Physikalisch-Technische Bundesanstalt, Braunschweig, Germany

<sup>b</sup>Technical University of Braunschweig, Institute of Production Metrology, Braunschweig, Germany

**Abstract.** We present an interferometric form measurement system that is capable of measuring the form of optical surfaces from flats to moderately curved freeforms. A Fizeau interferometer is scanned over the specimen measuring its topography and the distance to the surface in sub-aperture measurements. The angle between the interferometer and the specimen is adjusted for each position and additionally relevant stage angle errors are measured with two tiltmeters. An optical surface with a spherical form (50 mm diameter, 10 m radius of curvature) is measured, and an uncertainty budget yields an uncertainty of 69 nm ( $k = 2$ ) for its topography. The determined radius of curvature agrees well with the nominal specifications and a measurement with a coordinate measurement machine. Furthermore, a form measurement of a car's side window is presented. © The Authors. Published by SPIE under a Creative Commons Attribution 4.0 International License. Distribution or reproduction of this work in whole or in part requires full attribution of the original publication, including its DOI. [DOI: [10.1117/1.OE.61.9.094102](https://doi.org/10.1117/1.OE.61.9.094102)]

**Keywords:** interferometry; stitching; cavity length; wavelength sweeping; freeform; metrology.

Paper 20220505G received May 12, 2022; accepted for publication Aug. 17, 2022; published online Sep. 14, 2022.

## 1 Introduction

Stitching interferometry<sup>1</sup> enables the form measurement of optical surfaces that are too large or too strongly curved for a single measurement. Surfaces can be reconstructed by combining several subaperture measurements, which are again within the specifications of the respective interferometer. In modern instruments, wavelength-swept interferometry is used with Fizeau- or Michelson-type interferometers. An overview of state-of-the-art wavelength-swept interferometry can be found in Ref. 2.

For freeform optics,<sup>3</sup> stitching interferometry offers a flexible measurement capability. There are many types of reference wavefronts, measurement methods, and stitching algorithms. Some of these are listed in the following paragraphs.

One of the first setups for stitching interferometry was presented in Ref. 4. It combines a high-precision motion system with an interferometer to measure the form of near-spherical specimens. For subaperture stitching, parameters are introduced to correct global errors (reference wave, pixel scale and distortion) and local errors (angular and positional misplacement) of the subapertures.

A stitching interferometry setup for specimens up to about half an inch with large slopes was demonstrated in Ref. 5. A reference flat is used, and the specimen is positioned and tilted by a hexapod. The length gauges of its linear actuators give the angular and positional relation between the subaperture measurements. Another stitching interferometry method with a spherical reference wavefront is presented in Ref. 6 measuring a specimen with 100 mm in diameter and up to 1300  $\mu\text{m}$  of freeform departure from the best-fit sphere. Reference 7 presents an approach with a combination of subaperture stitching and white-light interferometry. Instead of tilting the specimen or the interferometer for larger slopes, a higher magnification is used

---

\*Address all correspondence to Jan Spichtinger, [jan.spichtinger@ptb.de](mailto:jan.spichtinger@ptb.de)

to resolve the interferograms. Therefore, the measurement time increases along with an increasing slope.

For aspheres, a Fizeau interferometer with a spherical reference wavefront can be used to scan the specimen along the optical axis to measure annular subapertures, e.g., in Ref. 8.

Apart from stitching interferometry, there are other methods for the measurement of optical surfaces with large curvatures. One example is computer-generated holograms,<sup>9</sup> which have to be created for each specific specimen form. They are used for repeated measurements of specimens with the same design. Another example is the tilted wave interferometer,<sup>10,11</sup> which uses spatially distributed light sources (instead of a positioning system) to determine a surface topography from several interferograms. The surface form is reconstructed by recreating the observed interference patterns with a numerical simulation of the system, thus solving an inverse problem.

For slightly curved but large specimens, e.g., synchrotron mirrors, other measurement setups are employed. For the form measurement of synchrotron x-ray mirrors, several stitching methods at the European Synchrotron Radiation Facility are reviewed in Ref. 12. One of those was for a specimen with a radius of curvature of 120 m. Here, the reproducibility of the radius of curvature remains an issue. In Ref. 13, stitching interferometry is used with a fixed Fizeau interferometer and a specimen on a linear scanning stage moving relative to the interferometer. Two tiltmeters are used to correct guideway errors of the linear stage. A method with self-referencing stitching interferometry on a two-dimensional (2D) profile, called traceable multiple sensor, was demonstrated for nearly flat surfaces.<sup>14</sup> Here, the angular position of the specimen is measured with an autocollimator.

Non-interferometric methods for high-accurate form measurement include deflectometry. Two examples are the software configurable optical test system (SCOTS)<sup>15</sup> and slope-measuring portable optical test system (SPOTS)<sup>16</sup> methods developed at the University of Arizona. SCOTS relies on a screen displaying a pattern and a camera as detection, whereas the SPOTS method uses an additional optic in the detection path. Another method<sup>17</sup> uses an autocollimator as a measuring head on a scanning stage to measure the slope of the surface under test with high accuracy. The measurement is limited to 2D profiles, but multiple profiles can be combined to get a three-dimensional (3D) topography.

A further option for measuring free-form surfaces is scanning profilometry, which is readily available with commercial setups. Examples include the NANOMEFOS<sup>18</sup> [developed by TNO (Netherlands Organisation for Applied Scientific Research) and Dutch United Instruments] and the LUPHOScan<sup>19</sup> (by Taylor Hobson), both of which employ optical probes, and the UA3P<sup>20</sup> (by Panasonic), which uses a tactile probe.

Our proposed method aims to measure specimens from optical flats to moderately curved surfaces, which can have arbitrary surface forms like freeforms or symmetrical forms. The maximum slope is limited by the interferometer. In Sec. 7, we show a measurement of a specimen with local radii of curvature down to  $\sim 2$  m.

We use a five-axis positioning system with three linear stages and two rotation stages to scan a specimen with a Fizeau interferometer. Two tiltmeters measure the guideway errors of two horizontal linear stages for the lateral positioning. An autocollimator measures the angle of the vertical linear stage and the two rotation stages carrying the interferometer. Alternatively, the rotation encoders of the rotation stages can be used. This determines the complete angle between the specimen and the interferometer. Furthermore, the distance between the surface and the interferometer is measured.

From this information, the subtopographies can be arranged in a global coordinate system. The lateral positions of the subtopographies are approximately accurate, but height differences between them still remain. This allows the stitching algorithm to be formulated in terms of a linear least squares problem limited to the vertical direction. The linearity is beneficial for the traceability of the form measurement.

One of the main advantages of the presented method is that it provides a very accurate measurement of the absolute form and curvature. The reason for this is that the inclinations of the subapertures are not adjusted during stitching since they are known from the angle measurement. Therefore, unknown systematic form errors of the interferometer's reference surface can only be accumulated as linear errors over the stitched topography but not as quadratic or higher order errors. Additionally, no calibration object is required, as is often used for scanning profilometry.

Another advantage of this method is that it can measure arbitrary surface forms (and shapes) as long as the maximum local gradients are still measurable. This means that the samples are not limited to spherical and aspherical forms with moderate free-form components.

It was developed from the traceable multiple sensor method,<sup>14</sup> from which the relative angle measurement between the interferometer and the specimen was adapted. The rotations of the interferometer extend the maximum slope of the specimens. The self-referencing of the reference surface was omitted for the time being since it plays a minor role compared to other errors. In addition, the transition from two-dimensional measurements of profiles to 3D measurements was made. The use of the tiltmeters to measure the angular errors of the linear stages is realized as in Ref. 13. A self-calibration of the systematic form errors of the reference flat as in Ref. 4 or Ref. 14 can also be implemented in this method.

## 2 Methods

### 2.1 Setup

A schematic drawing of the setup is shown in Fig. 1, and an image of the actual setup is shown in Fig. 2. The optical measurement head is a Fizeau interferometer (model: VI-direct 10 by Möller-Wedel GmbH & Co. KG) with an aperture of 10 mm, an image sensor with  $1600 \times 1200$  pixels and a reference flat. The frequency of the laser (model: LaSy 633 by TEM Messtechnik GmbH) for the Fizeau interferometer can be swept in the range of 300 GHz (corresponding to a wavelength range of 0.4 nm) around the central wavelength of 633 nm. The specimen is placed on the lower linear y-stage (custom built). The x-stage (manufacturer: PI Micos GmbH) bears a tower with a rotation stage and a goniometer (manufacturer: Newport Corporation) to carry the Fizeau interferometer. They share a common pivot point and can tilt the interferometer to align it to the specimen gradient in its field of view. The Fizeau interferometer can also be adjusted in height with a linear z-stage (manufacturer: Newport Corporation) to be focused on the surface because it has a fixed focal length. The mechanical stability of the structure carrying the interferometer was verified with an autocollimator. The measurement area given by the travel range of the x- and y-stage is  $1000 \text{ mm} \times 200 \text{ mm}$ .

The tiltmeters measure the angular guideway errors of the linear x- and y-stages. The autocollimator measures the angular position of the Fizeau interferometer relative to the x-stage. For larger rotations, the angular position is also known from the rotation encoders; however, this is less accurate. Thus, the complete angular relation of the specimen and the interferometer is known. The relative position is known from the length gauges of the linear stages.

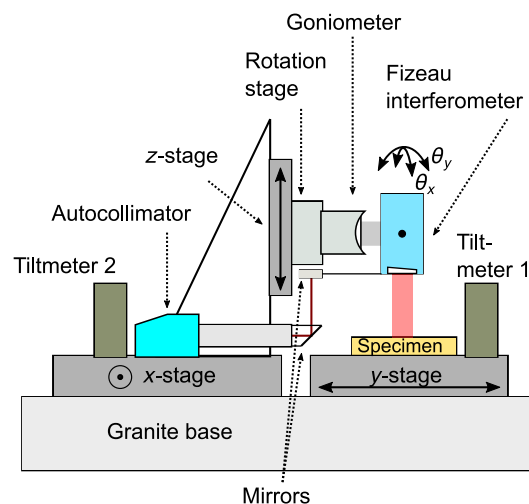


**Fig. 1** Schematic drawing of the measurement setup.

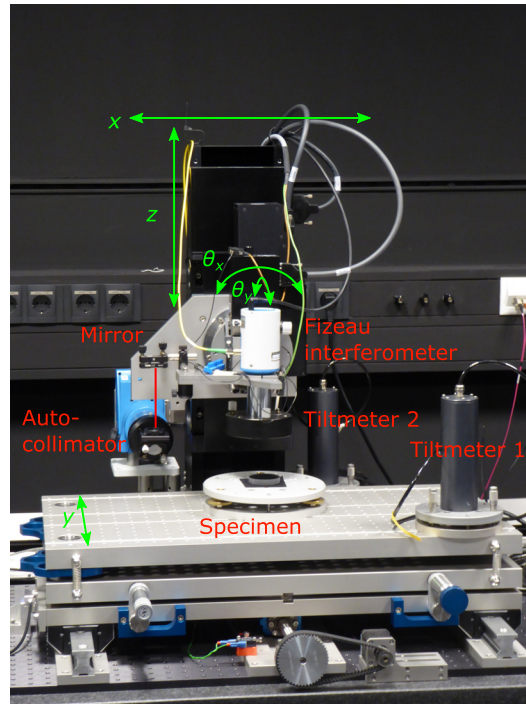


**Fig. 2** Photo of the measurement setup.

The vertical distance from the pivot point to the reference flat  $d_{\text{RF-PP}}$  must be known for the stitching and can be geometrically determined. A reflective specimen with a marker is placed under the Fizeau interferometer. The distance  $d$  from the reference flat to the specimen is measured with wavelength-swept interferometry (see Sec. 2.2). Then the Fizeau interferometer is rotated by a certain angle  $\gamma$  with one of the rotation stages. The distance  $d_{\text{RF-PP}}$  can be calculated from the lateral displacement  $d_{\text{lat}}$  of the marker, the angle  $\gamma$  and the distance  $d$ :

$$d_{\text{lat}} = (d_{\text{RF-PP}} + d) \tan(\gamma), \quad (1)$$

$$\Leftrightarrow d_{\text{RF-PP}} = \frac{d_{\text{lat}}}{\tan(\gamma)} - d. \quad (2)$$

The lateral position of the pivot point is not critical, as long as the tilt angles of the interferometer are small.

## 2.2 Wavelength-Swept Interferometry

The Fizeau interferometer utilizes the tunable laser with a wavelength range of 0.4 nm. The electromagnetic waves reflected from the specimen and the reference flat interfere with each other. During the wavelength sweep, the intensity is measured (see Fig. 3). From the Fourier spectrum, the wrapped phase  $\phi_{\text{wrapped}}(x, y)$  and the frequency of the interference signal can be calculated for every pixel (see Fig. 4).

The phase map is unwrapped with a 2D unwrapping algorithm<sup>21</sup> to obtain the continuous phase map  $\phi(x, y)$ . The topography of the specimen is then given as

$$z(x, y) = \frac{\lambda \phi(x, y)}{2 \cdot 2\pi}, \quad (3)$$

where  $\lambda$  is the central wavelength of the laser. The cavity length, i.e., the absolute distance from the reference flat to the surface, is given by [see e.g., Eqs. (1) and (2) in Ref. 22]

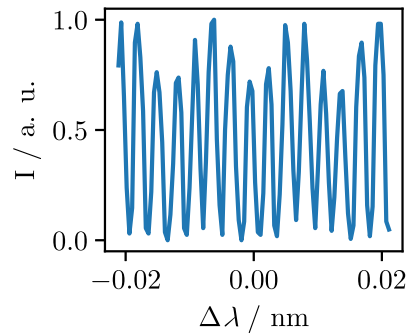


**Fig. 3** This figure shows part of the intensity signal during the wavelength sweep at one pixel of the interferometer. The dominant frequency and its phase can be determined by Fourier analysis (see Fig. 4).

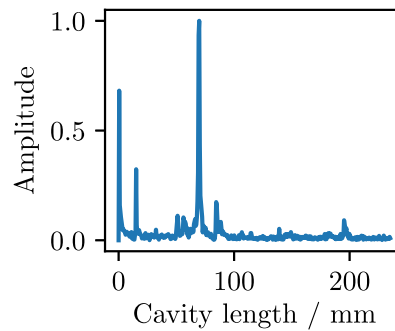


**Fig. 4** This plot shows the absolute value of the Fourier transform of the signal in Fig. 3. The peak with the highest amplitude corresponds to the cavity formed between the reference flat and the specimen. The phase of this oscillation gives the topography.

$$d = \frac{\lambda^2}{\Delta\lambda} \frac{\Delta\phi}{4\pi}. \quad (4)$$

This formula can be rearranged as

$$d = \frac{1}{2} \lambda^2 \nu, \quad (5)$$

where  $\nu$  is the dominant frequency obtained from the Fourier spectrum, which describes how the phase of the interference signal changes by  $\Delta\phi$  for a wavelength sweep  $\Delta\lambda$ :

$$2\pi\nu = \frac{\Delta\phi}{\Delta\lambda}. \quad (6)$$

### 2.3 Subaperture Measurements

A specimen that has a larger aperture diameter than the interferometer has to be measured in many subaperture measurements that overlap with each other in the  $xy$ -plane. The positioning system moves the interferometer from position to position on a raster path (see Fig. 5). In the measurement presented later, the step size is 5 mm, and the effective aperture size is 8 mm. A single subaperture measurement is done in the following way: First, a single image from the interferometer is taken to check if the specimen is within the field of view at this position. Then an interferometric measurement is performed. The relative angle between the specimen and the interferometer is determined from the obtained topography, and compensated for with the two rotation stages. The correct focal distance is set with the vertical  $z$ -stage using the measured absolute distance. After the adjustment, the interferometric measurement is repeated, and the new values of topography and distance are stored. The measurement values of the tiltmeters and the autocollimator are also stored. The geometry of a subaperture measurement is shown in

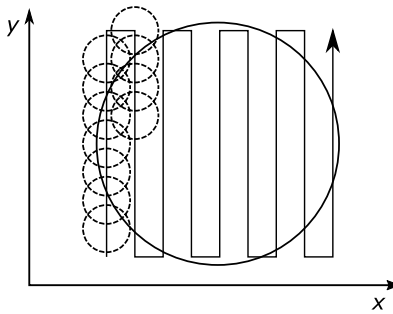


**Fig. 5** The large circle is a specimen from the top view. The Fizeau interferometer is moved along the raster path. In equidistant steps, an interferometric measurement is performed. The first 11 measurement areas starting from the bottom left are depicted by the dashed circles.

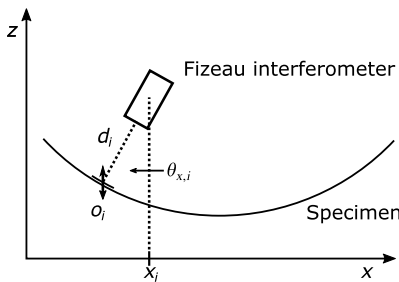


**Fig. 6** The Fizeau interferometer measures the subtopography of the specimen at the  $i$ 'th position. Due to the several measurement uncertainties, the subtopography's position in space is not exactly known. The resulting offset  $o_i$  is fitted in the vertical direction, approximating a fit along  $d_i$ . The position  $x_i$  is measured with a linear encoder.

Fig. 6. All stages approach all positions unidirectionally to achieve the maximal position repeatability.

## 2.4 Subaperture Stitching with Absolute Distance Measurement

The complete surface form has to be reconstructed from the subaperture measurements. The distance from the interferometer to the specimen has been measured with each subaperture measurement. The best achievable uncertainty of the absolute distance measurement amounts to  $\sim 30 \mu\text{m}$ , and therefore, is magnitudes of orders worse than that of the topography measurement, which is only relative. Therefore, adjacent subtopographies may have a height difference. When the Fizeau interferometer is tilted with the rotation stages, its optical axis is not parallel to the  $z$ -stage anymore. Therefore, the uncertainty of the distance measurement may also cause a lateral displacement of adjacent subtopographies. However, the tilt angles  $\theta_{x,i}$  and  $\theta_{y,i}$  are small so that this lateral displacement is neglected. With an uncertainty of  $30 \mu\text{m}$  for the distance measurement, the resulting uncertainty of the lateral position would be  $2.6 \mu\text{m}$  at an angle of  $5^\circ$ . The height differences of overlapping subtopographies can be corrected by means of a linear equation system, minimizing the sum of the quadratic height differences.

The quantities used for the stitching are shown in Fig. 7. First, all pairs of subtopographies that are close to each other in the  $xy$ -plane are searched for. The point coordinates of a first subtopography that lie within the convex hull enclosing the coordinates of a second are identified to find the area of overlap. The points of the two different measurements are generally not on the same grid. Therefore, the height values of the second topography are linearly interpolated at the lateral coordinates of the first. Then the mean height of the points of each subtopography in the area of overlap is calculated.

Subsequently, the linear equation system can be set up with the following equation for each overlap of two subtopographies  $i$  and  $j$ :

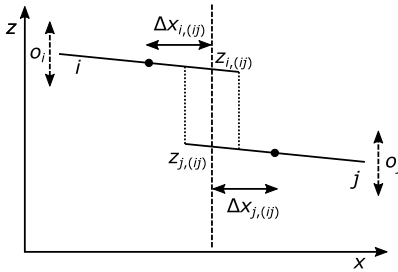


**Fig. 7** The two subapertures  $i$  and  $j$  overlap in the  $xy$ -plane. The dots are the centers of each topography. The long dashed line is the center of the overlapping region in the  $x$ -direction. The  $y$ -direction is treated equivalently.  $z_{i,(ij)}$  and  $z_{j,(ij)}$  are the mean heights in the overlapping region.  $\Delta x_{i,(ij)}$  and  $\Delta x_{j,(ij)}$  are the  $x$ -distances from the center of the topographies to the center of the overlapping area. The dashed arrows show how the offset parameters  $o_i$  and  $o_j$  shift the subapertures.

$$[z_{i,(ij)} + o_i] - [z_{j,(ij)} + o_j] = 0, \quad (7)$$

where  $z_{i,(ij)}$  are the mean height values of the  $i$ 'th subtopography (indicated by the first part of the index  $i$ ) in the region of overlap with the  $j$ 'th measurement [indicated by  $(ij)$ ], and vice versa for  $z_{j,(ij)}$ .  $o_i$  and  $o_j$  are the height offsets to be determined. Since there are more overlaps than subapertures, it is an overdetermined system and a linear least-squares solution can be found. The complete topography is obtained by adding the determined offsets  $o_i$  to the subtopographies.

Figure 8 shows how flat subtopographies with a symmetrical systematic error are stitched together.

The stitching already works in this simple version, but it can be improved with a parameter for the adjustment of the autocollimator measuring  $\theta_{x,i}$  and  $\theta_{y,i}$ . The parameter describes the rotation  $\alpha$  of the autocollimator around its optical axis due to an imperfect adjustment. The autocollimator ideally measures the two angles  $\theta_x$  and  $\theta_y$  of the mirror attached to the Fizeau interferometer. If it is not perfectly aligned, the measured angles (marked with a single quotation mark) contain part of the perpendicular angle:

$$\theta'_x = \theta_x \cos(\alpha) + \theta_y \sin(\alpha), \quad (8)$$

$$\theta'_y = \theta_y \cos(\alpha) - \theta_x \sin(\alpha). \quad (9)$$

The cosine terms are approximately equal to 1 because the adjustment error is small. These angles are already considered when placing the subtopographies in space. The sine terms can be simplified to  $\sin(\alpha) \approx \alpha$  in the small angle approximation.

The linear equation system from Eq. (7) is extended with the height differences resulting from the angle product  $\alpha\theta_{x,i}$  multiplied by  $\Delta x_{i,(ij)}$  (see Fig. 7) and the corresponding terms for the other subapertures in the  $x$ - and  $y$ -direction.

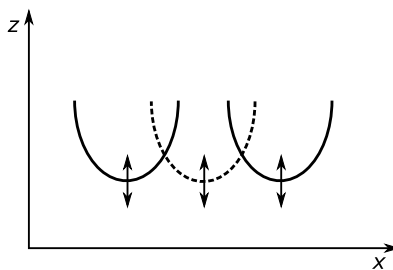


**Fig. 8** A 2D view from the side showing how three actually flat subtopographies with a spherical form error of the reference flat are stitched. The symmetrical systematic errors only cause local errors in the stitched topography because the tilts are fixed.

$$[z_{i,(ij)} + o_i + \alpha\theta_{x,i}\Delta x_{i,(ij)} - \alpha\theta_{y,i}\Delta y_{i,(ij)}] - [z_{j,(ij)} + o_j + \alpha\theta_{x,j}\Delta x_{j,(ij)} - \alpha\theta_{y,j}\Delta y_{j,(ij)}] = 0, \quad (10)$$

where  $\Delta x_{i,(ij)}$  is the  $x$ -distance from the center of the subaperture measurement of the subaperture  $i$  to the center of the  $xy$ -overlap of the topographies  $i$  and  $j$ .  $\theta_{x,i}$  is the measured angle in the  $x$ -direction for the  $i$ 'th subaperture. The linear equation system can be simplified to

$$[z_{i,(ij)} + o_i] - [z_{j,(ij)} + o_j] + \alpha c_{ij} = 0. \quad (11)$$

The parameter  $c_{ij}$  summarizes the effects of a rotation of the autocollimator on the mean height difference in the overlapping region:

$$c_{ij} = [\theta_{x,i}\Delta x_{i,(ij)} - \theta_{y,i}\Delta y_{i,(ij)}] - [\theta_{x,j}\Delta x_{j,(ij)} - \theta_{y,j}\Delta y_{j,(ij)}]. \quad (12)$$

To obtain the complete topography, the offsets  $o_i$  and the tilts caused by the autocollimator adjustment parameter are added to the subtopographies.

### 3 Experimental Results

A spherical specimen was measured as a proof of principle. It had a diameter of 50.8 mm, was made of BK7, and was also uncoated (manufacturer: Eksma Optics). The radius of curvature was specified with  $10 \text{ m} \pm 0.1 \text{ m}$ . The whole specimen was measured with 99 subapertures and a lateral step size of 5 mm in  $x$  and  $y$ . The inner 8 mm of the 10 mm aperture of the interferometer was used because there are faint interference fringes at the edge of the aperture caused by the device itself. The data from the image sensor was subsampled to an effective pixel pitch of  $17.3 \mu\text{m}$  to reduce the computation time without significantly reducing the accuracy of the measurement. This corresponds to about 167,000 pixels in a subaperture. The measurement took about two hours.

A total of 170 overlapping areas were found that contained at least 100 valid pixels. The subtopographies were stitched with the equation system from Eq. (11) in Sec. 2.4. The autocollimator adjustment parameter was determined to  $\alpha = 0.158 \text{ deg}$ . The estimated standard error of the regression (i.e., the root of the residual variance) for the height offsets  $o_i$  of the subtopographies was  $\text{SER} = 2.8 \text{ nm}$ . The stitched topography was described by a point cloud with unevenly spaced points due to the higher points density in the overlapping regions. The point cloud was linearly interpolated on a grid with  $250 \times 250$  points with a resulting lateral distance of  $191.61 \mu\text{m}$ . The global tilt of the whole topography was fitted and subtracted. The reconstructed topography is shown in Fig. 9.

A spherical function was fitted to the topography with a nonlinear least-squares fit to compare the result with the nominal radius of curvature. Only the inner 48 mm of the topography were used because the topography deviated from the spherical form close to the edge. The fit yielded a radius of curvature of  $9.9936 \text{ m}$ . The respective standard deviation calculated from the covariance matrix of the fit was  $0.5 \text{ mm}$ . This value lies well within the nominal radius of

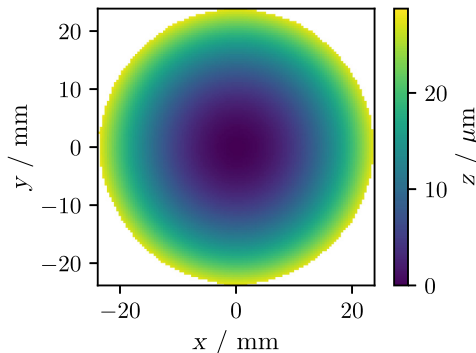


**Fig. 9** The figure shows the inner 48 mm of the topography. The spherical form is clearly visible. It has a PV height of  $h_{\text{PV}} = 28.74 \mu\text{m}$ .

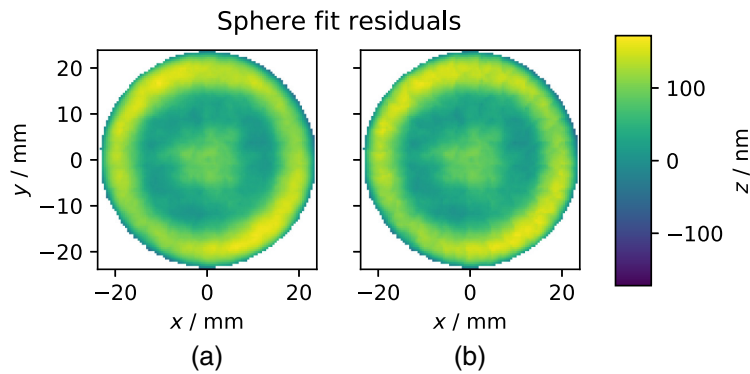


**Fig. 10** (a) This figure shows the topography after subtracting the best-fit sphere. The residual of the fit has a rotationally symmetric form, which is a typical artifact from the manufacturing process. The circular artifacts are mainly caused by small tilt errors of the subapertures. (b) Without the adjustment parameter for the autocollimator, the artifacts are visible at the edges of the subtopographies due to an additional tilt error of the individual subapertures [compare to (a)]. The artifacts have PV heights of up to 30 nm.

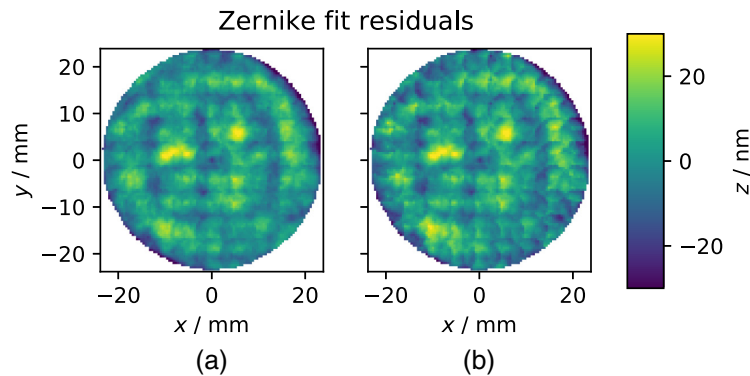


**Fig. 11** Fit residuals after removal of the first 36 Zernike polynomials. (a) With the adjustment parameter, the RMS value of the residual is 8.7 nm. (b) Without the adjustment parameter, the RMS value amounts to 9.9 nm. It can be seen that the subapertures have a more pronounced tilt error in tangential direction than in (a).

$10 \text{ m} \pm 0.1 \text{ m}$ . The best-fit sphere was subtracted from the topography for further evaluation. The fit residual is shown in Fig. 10(a). Its form resembles the spherical aberration term of the Zernike polynomials. The RMS height of the fit residual is 57 nm. There are also slight circular artifacts in the residuum because the subtopographies do not perfectly match in the stitching.

To demonstrate the effects of the adjustment parameter for the autocollimator, the stitching was repeated without this parameter, i.e., according to Eq. (7). In Fig. 10(b), the artifacts due to the tilt errors can be seen, especially at the edges of the subtopographies.

To make the effect of the adjustment parameter for the autocollimator more obvious, the first 36 Zernike polynomials were fitted and subtracted from the topographies. The results can be seen in Figs. 11(a) and 11(b).

#### 4 Uncertainty Budget

To complete the measurement in Sec. 3, an uncertainty budget was set up. The aim was to quantify the most relevant uncertainty contributions, but not to develop an all-encompassing uncertainty budget. Several contributions were dependent on the specimen topography, meaning that their values were specific for this specimen.

### 4.1 Uncertainty of the Topography Measurement

To estimate the uncertainty of the topography measurement for an arbitrary specimen, two of the most distant points with the largest curvature between are chosen. The combined uncertainty for their relative height contains the uncertainty components of their respective subaperture measurement and of the direct path connecting them. For the spherical specimen, the longest direct path is along the diameter in any direction and consists of 10 subapertures so that there are  $N_{\text{path}} = 9$  overlaps of subtopographies between the outer two subtopographies.

A model equation for the determination of the measurement uncertainty of the measured topography  $z(x, y)$  can be described as

$$z(x, y) = z_k(x, y) - z_r(x_r, y_r) + \sum_{s=1}^{N_{\text{path}}} \Delta z_s. \tag{13}$$

The first term  $z_k(x, y)$  describes the first point of the topography that belongs to the subtopography  $k$ . The second term describes the second point chosen as reference point  $z_r(x_r, y_r)$  in a subtopography  $r$ . The heights of both points are relative to their respective subtopography. The third term describes the sum of the height differences  $\Delta z_s$  that occur for each stitched subtopography  $s$  on the path between  $z_k(x, y)$  and  $z_r(x_r, y_r)$ .  $z_r(x_r, y_r)$  is subtracted from the other two terms to get the topography  $z(x, y)$  relative to this reference point.

From the model equation, the uncertainty can be calculated as follows:

$$u(z)^2 = u(z_k)^2 + u(z_r)^2 + u\left(\sum_{s=1}^{N_{\text{path}}} \Delta z_s\right)^2. \tag{14}$$

The terms  $u(z_k)$  and  $u(z_r)$  are equal because they describe the uncertainty for a single subaperture measurement. The equation can be shortened to

$$u(z)^2 = 2 \cdot u(z_k)^2 + u\left(\sum_{s=1}^{N_{\text{path}}} \Delta z_s\right)^2. \tag{15}$$

The uncertainty component  $u(z_k)$  for the single subaperture measurement can be split up into a lateral and a height uncertainty component

$$u(z_k)^2 = u_{\text{lateral}}(z_k)^2 + u_{\text{height}}(z_k)^2. \tag{16}$$

In principle, interactions of several input quantities may occur. However, they are typically small and can be neglected.

In the following sections, several important input quantities are discussed and summarized in Table 1.

**Table 1** Uncertainty budget of  $u_z(x, y)$  with the most important contributions to the measurement of the spherical specimen. The estimates of all quantities are zero.

Quantity	Uncertainty	Distribution	Sensitivity coefficient	Uncertainty contribution
Reference flat <sup>a</sup>	21 nm	Rectangular	1	6.1 nm
Distortion <sup>a</sup>	8.64 μm	Normal	$R_{\text{subaperture}}/r_C$	4 nm
Lateral position <sup>a</sup>	8.2 μm	Normal	$\theta_{\text{max}}$	20.5 nm
Angle <sup>a</sup>	2.1 μrad	Normal	$R_{\text{subaperture}}$	8.4 nm
Stitching	2.8 nm	Normal	$\sqrt{N_{\text{overlap}}}$	8.4 nm
Combined uncertainty	—	—	—	34.1 nm ( $k = 1$ )

<sup>a</sup>The components for are counted twice to account for the factor in Eq. (15).

#### 4.1.1 Lateral uncertainty component $u_{\text{lateral}}(z_k)$ of the single subtopography

First, the lateral positioning of the subtopographies is considered. For simplicity, the equation is set up for one dimension, but it is valid for the whole specimen because of its symmetry. The uncertainty  $u(x)$  of the  $x$ -coordinate is given as

$$u(x)^2 = u_{y\text{-stage}}(x)^2 + u_{z\text{-stage}}(x)^2 + u_d(x)^2 + u_{\theta_x}(x)^2. \quad (17)$$

1. The straightness of the  $y$ -stage in the  $x$ -direction is given by  $20 \mu\text{m}$  (peak-to-valley). The corresponding uncertainty is  $u_{y\text{-stage}}(x) = 20 \mu\text{m}/\sqrt{12}$ .
2. The second term  $u_{z\text{-stage}}(x) = 20 \mu\text{m}/\sqrt{12}$  is the equivalent of the  $z$ -stage.
3.  $u_d(x) = u(d) \sin(\theta_{\text{max}})$  is the uncertainty component for the absolute distance measurement. With  $u(d) = 100 \mu\text{m}$  and a maximum rotation of the interferometer  $\theta_{\text{max}} = 0.3 \text{ deg}$ , it follows that  $u_d(x) = 0.6 \mu\text{m}$ .
4.  $u_{\theta_x}(x)$  is the combined uncertainty for the angle measurement of the two tiltmeters with  $u_{\text{TM}}(\theta_x) = 0.25 \text{ arcsec}$  each and the autocollimator with  $u_{\text{AC}}(\theta_x) = 0.25 \text{ arcsec}$ . It amounts to  $u_{\theta_x}(x) = 0.45 \text{ arcsec} = 2.1 \mu\text{rad}$ . With an approximate distance from the pivot point to the specimen of  $200 \text{ mm}$ , it amounts to  $u_{\theta_x}(x) = 0.5 \mu\text{m}$ .

The dominating uncertainties are the straightness of the linear stages by about one order of magnitude. The maximum resulting topography uncertainty can be estimated by a multiplication with the maximum gradient of the specimen  $(\frac{dz}{dx})_{\text{max}} = \frac{R_{\text{specimen}}}{r_c} = \frac{50.8 \text{ mm}/2}{10 \text{ m}}$ :

$$u_{\text{lateral}}(z) = u(x) \cdot \left(\frac{dz}{dx}\right)_{\text{max}}. \quad (18)$$

This yields a contribution of  $u_{\text{lateral}}(z) = 20.5 \text{ nm}$  for  $u(x) = 8.2 \mu\text{m}$ . The maximum gradient was obtained by using the parabolic approximation to a spherical surface with  $z(x) = \frac{x^2}{2r_c}$ . Contributions of the eccentricity and wobble of the rotation stages and the position of the pivot point are neglected because they are small due to the small angle range. The Abbe error for the distance from the Fizeau interferometer and the specimen to the respective linear encoder is also one order of magnitude smaller than the straightness and therefore neglected.

In addition, the uncertainty contribution from the distortion of the imaging optics is considered. The distortion of the Fizeau interferometer was determined to be  $<1$  pixel or  $8.64 \mu\text{m}$  for the total aperture of  $10 \text{ mm}$ . The maximum gradient within the  $4 \text{ mm}$  radius is  $(\frac{dz}{dx})_{\text{max}} = \frac{R_{\text{subaperture}}}{r_c} = \frac{4 \text{ mm}}{10 \text{ m}}$ . The maximum height uncertainty contribution to  $u_{\text{lateral}}(z)$  according to Eq. (18) is  $4 \text{ nm}$ .

#### 4.1.2 Height uncertainty component $u_{\text{height}}(z_k)$ of the single subtopography

Here, input quantities that directly influence the height values are discussed.

1. The reference flat of the Fizeau interferometer has a flatness deviation of  $\frac{\lambda}{30} \approx 21 \text{ nm}$ . This is a manufacturer's specification, which was confirmed with a measurement relative to a flat with a nominal flatness error of  $\frac{\lambda}{100}$ . The quadratic component is about  $1 \text{ nm}$  peak-to-valley. This value divided by  $\sqrt{12}$  is taken as the corresponding uncertainty component  $u_{\text{RF}}(z)$ .
2. The uncertainty of the angle measurement  $u(\theta)$  causes a tilt uncertainty of a subtopography that results in a local height uncertainty of  $u_{\theta}(z_k) = u(\theta) \cdot R_{\text{subaperture}} = 8.4 \text{ nm}$ .

This leads to

$$u_{\text{height}}(z_k)^2 = u_{\text{RF}}(z_k)^2 + u_{\theta}(z_k)^2 \approx 10.4 \text{ nm}. \quad (19)$$

Uncertainty components that are small and not included here are the repeatability of the subaperture measurement, the retrace error, camera noise and the laser wavelength. Effects of the retrace error in stitching were studied in Ref. 23, however, for a different stitching algorithm.

#### 4.1.3 Uncertainty component $u\left(\sum_{s=1}^{N_{\text{path}}} \Delta z_s\right)$ for the stitching

The least-squares solution to the linear stitching problem has an estimated standard error of the regression of  $\text{SER} = 2.8$  nm. All residuals are smaller than 8 nm. There are  $N_{\text{overlap}} = 9$  overlaps along one direction. The total uncertainty is estimated to be

$$u\left(\sum_{s=1}^{N_{\text{overlap}}} \Delta z_s\right) = \sqrt{N_{\text{overlap}}} \cdot \text{SER} = 8.4 \text{ nm}, \quad (20)$$

for a profile through the center. The standard error of regression also contains any errors that cause the subtopographies to not fit perfectly in the overlapping region.

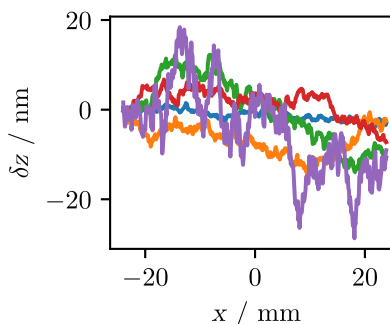
#### 4.1.4 Combined uncertainty $U(z)$

Table 1 shows the measurement uncertainty budget for the standard measurement uncertainty according to Eq. (15). This results in an expanded measurement uncertainty of  $U(z) = 69$  nm ( $k = 2$ ). The value of the measurand then normally lies within the attributed coverage interval with a probability of  $\sim 95\%$ .

#### 4.2 Uncertainty of the Radius of Curvature

In the next step, a brief Monte Carlo simulation was performed to evaluate the propagation of the topography uncertainty into the radius of curvature uncertainty.

In Sec. 4, it was assumed that the topography errors between two points of the topography are integrated over the lateral path between them. Therefore, modeling the topography error simply as Gaussian noise added to the topography would contradict this assumption. Instead, a random value from a normal distribution is drawn for each topography point. The random values are cumulated along the path between the two remotest points. The sum of the previous random values up to a certain position represents the topography error at this point. This process is equivalent to a one-dimensional Gaussian random walk where the steps are the lateral positions and the value for a step is the topography error at this position. The peak-to-valley (PV) height of the random walk is drawn from the normal distribution of the topography uncertainty with  $u(z) = 34.1$  nm from Sec. 4. One cycle of the Monte Carlo simulation is performed by adding a topography error created by the random walk to the ideal topography along the  $x$  axis for  $y = 0$  and determining the best-fit sphere for this profile. Five examples of outcomes of the random walk can be seen in Fig. 12. All in all, 10,000 repetitions have been performed leading to the distribution of radii shown in Fig. 13. The lateral resolution of the topography only marginally influences the uncertainty of the radius of curvature when it is in a reasonable range. This can be explained by the fact that the course of the random walk is not significantly influenced by the lateral sampling. The 95% coverage interval for the radius of curvature is given by  $[r_C - 9 \text{ mm}, r_C + 9 \text{ mm}]$ .



**Fig. 12** Five examples of the topography error in the Monte Carlo simulation. The offsets are irrelevant because they are also fitted while determining the best-fit sphere.

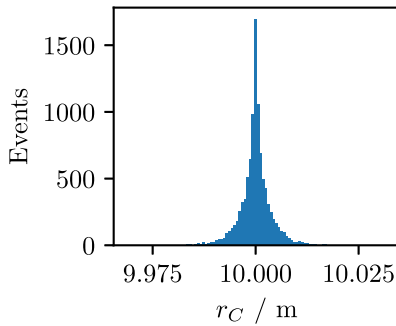


**Fig. 13** Histogram showing the best-fit radii of curvature for 10,000 different random walks added to the ideal profile at  $y = 0$ .

## 5 Comparison with a Scanning Stage with a Chromatic Confocal Sensor

In this section, the stitching interferometry measurement was compared to a measurement with a chromatic confocal sensor (Precitec CHRocodile 2 S). The sensor was attached to the  $x$ -stage of the positioning system from Sec. 2.1. It had a measurement range of  $300 \mu\text{m}$  and a working distance of  $4.5 \text{ mm}$ . The height resolution was  $10 \text{ nm}$  and the accuracy  $100 \text{ nm}$ . To find the center of the specimen, a scan in the  $y$ -direction of the system was performed. The points with the first and last valid measurement on the edges of the specimen were sought with a resolution of  $50 \mu\text{m}$ . The mean values of these  $y$ -coordinates gave the  $y$ -position, where an  $x$ -scan passed through the center of the specimen. The  $x$ -scan was performed in steps of  $100 \mu\text{m}$ . At each position, 10 chromatic confocal measurements were averaged. The scan took about 30 min. The resulting 2D profile was filtered with a Gaussian filter with  $\sigma = 100 \mu\text{m}$  to suppress noise. Also, a reference measurement of a nearly flat surface was subtracted to correct for stage errors. The profile is shown in Fig. 14.

The tilt was subtracted from the 2D topography, and a sphere was fitted to the data using nonlinear least squares. The  $y$ -coordinate was assumed to be zero. The fit yielded a radius of curvature of  $9.983 \text{ m}$  with a standard deviation of  $4 \text{ mm}$  calculated from the variance of the radius in the covariance matrix. The Gaussian filter applied earlier changed the radius of curvature by  $<1 \text{ mm}$ . The residuum after the subtraction of the best-fit sphere (Fig. 15) had an RMS height of  $66 \text{ nm}$ . The small local maximum at the center of Fig. 10(a) can also be seen, but it is superimposed by the remaining height errors of the scanning stage. The straightness of the  $1 \text{ m } x$ -stage is specified as  $20 \mu\text{m}$  (peak-to-valley). For the diameter of the specimen, the uncertainty contribution for the guideway (taking into account the reference measurement) is estimated to be  $u(h) = 100 \text{ nm}$ . This may again be converted to an uncertainty of the radius of curvature with a Monte Carlo simulation using the same method as in Sec. 4.2.

The 95% coverage interval for the radius of curvature is given by  $[r_C - 27 \text{ mm}, r_C + 27 \text{ mm}]$ . The coverage interval for the radius of curvature measured with the chromatic confocal

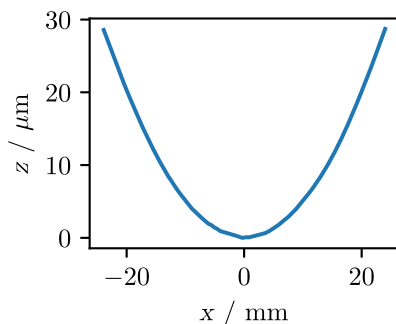


**Fig. 14** The topography of the specimen at  $y = 0$  measured with a chromatic confocal sensor mounted to a linear stage.

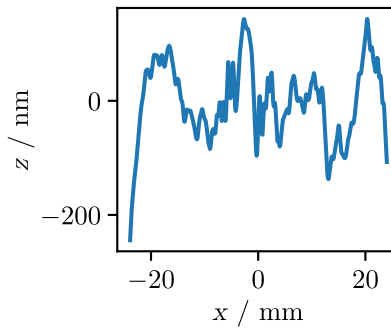


**Fig. 15** The residuum of the topography after a best-fit sphere is subtracted.

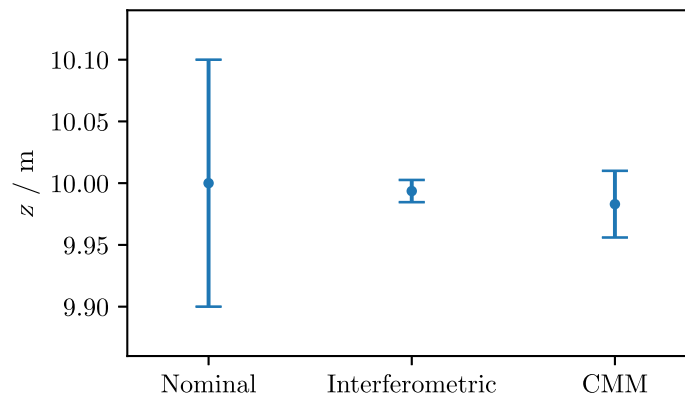


**Fig. 16** Comparison of the values for the radius of curvature of the spherical specimen. For the nominal value, the error bar is the specified tolerance range. For the interferometric measurement and the CMM measurement, the error bars indicate the expanded uncertainty ( $k = 2$ ).

sensor is larger compared to the one determined for the interferometric measurement in Sec. 4.2 due to the straightness error of the linear stage.

A graphical comparison of the specified and measured values for the curvature can be found in Fig. 16.

## 6 Traceability

In this section, we discuss how the result of the stitching interferometry measurement can be traced back to SI units. A possible traceability chain is shown in Fig. 17. At the moment, not all components of the setup have been calibrated yet.

The central wavelength of the interferometer laser with the iodine reference cell can be traced to the wavelength of an unstabilized He–Ne laser using a wavelength meter, for example. The He–Ne laser's wavelength at about 633 nm is one possible realization of the meter according to the recommendation of the Bureau International des Poids et Mesures.<sup>24</sup> The reference flat can be traced back to a three-flat test.<sup>25</sup> The linear encoders can be calibrated with a laser interferometer based on a He–Ne laser as a primary standard as well.

The rotation encoders and the autocollimator can be calibrated with an angle comparator<sup>26</sup> at a national metrology institute. The tiltmeters measuring the angle errors of the  $x$ - and  $y$ -stage can be calibrated with the autocollimator. A calibrated thermometer ensures that the temperature is within the temperature range permitted by the calibration of the system components. Any change of the refractive index of air due to environmental conditions is neglectable in this case. From here on, the subtopographies along with their positions and orientations are traceable and yield the complete topography. The choice of the stitching algorithm also influences the stitched topography and determines how the uncertainty contributions propagate into the topography.

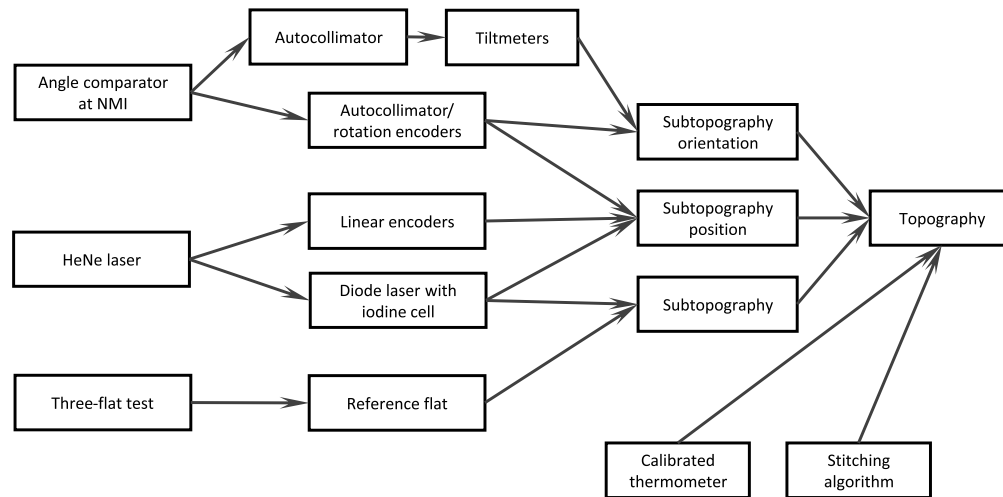


Fig. 17 One possible traceability chain for the form measurement presented.

## 7 Measurement of a Car's Side Window

Here, a measurement of a larger specimen in the form of a car's side window is presented as an example (see Fig. 18). The area of the side window is  $500 \times 230 \text{ mm}^2$ , of which  $500 \times 200 \text{ mm}^2$  are measured (due to the limited measurement area). Its freeform topography is about 4 mm high, and the radii of curvature are larger than 2 m. The measurement consists of 3100 subaperture measurements. The subaperture measurements are stitched according to Eq. (7) minimizing the mean height differences in the overlapping regions. The standard error of the regression is  $\text{SER} = 84 \text{ nm}$ . The stitched topography is shown in Fig. 19.

As a comparison, the profile marked with a green line in Fig. 18 was measured with a chromatic confocal sensor on a coordinate measurement machine (CMM). The resulting two-dimensional profile was fitted to the 3D interferometric topography measurement. Therefore, the lateral position and the orientation of the profile relative to the interferometrically measured topography were sought after by minimizing their RMS difference with the Nelder–Mead method. Due to the different grids of the two measurements, the 3D topography was interpolated with cubic splines at the points of the profile. Also, the tilt and offset were removed from the difference before calculating the RMS value. The best matching profiles of the CMM measurement and the interferometric measurement are shown in Fig. 20. The difference of the profiles is shown in Fig. 21. The RMS difference between the two measurements amounts to  $370 \text{ nm}$ , whereas the PV difference amounts to  $\pm 1 \mu\text{m}$ .

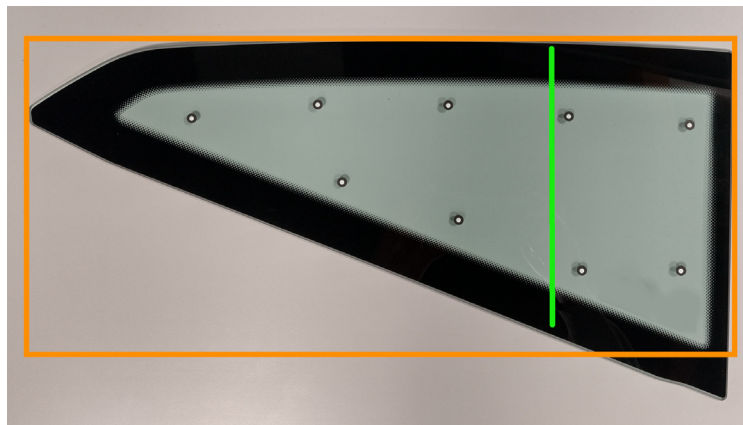
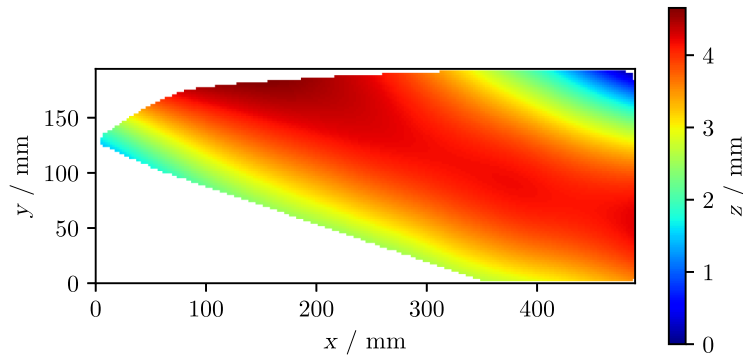
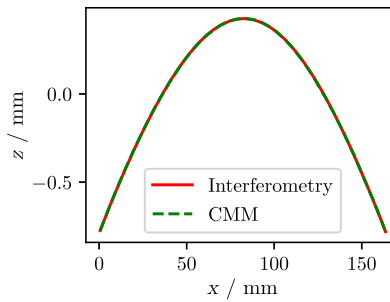


Fig. 18 Photo of the specimen that was measured. The orange box roughly marks the area that was measured. The green line gives the approximate position of a profile, which is later compared with a CMM measurement.



**Fig. 19** Topography of the car's side window stitched from 3100 subapertures.



**Fig. 20** The profile of the comparison measured with the two different methods.

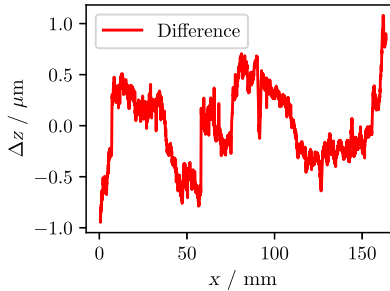


**Fig. 21** Difference of the matched profiles measured with the stitching interferometry and the CMM.

The uncertainty budget from Sec. 4 is transferred to this measurement. The specimen is not rotationally symmetric so the number of subapertures  $N$  depends on the profile that is evaluated. The profile that is compared with the CMM measurement consists of  $N_{\text{profile}} = 34$  overlaps. For this large specimen with many subapertures, it is assumed that all uncertainty contributions are implicitly contained in the uncertainty contribution for the stitching. The uncertainty is given by  $u_{\text{profile}}(z) \approx u(\sum_{s=1}^{N_{\text{overlap}}} \Delta z_s) = \sqrt{N_{\text{overlap}}} \cdot \text{SER} \approx 483 \text{ nm}$ . The comparison with the chromatic confocal sensor shows that more than 99.9% of the difference profile lies within the expanded measurement uncertainty of  $U(z) = 966 \text{ nm}$  ( $k = 2$ ).

To estimate the uncertainty of the whole topography, the longest edge length of 500 mm is considered. It consists of  $N_{\text{longest}} = 99$  overlaps. The uncertainty of the topography is given by  $u(z) \approx \sqrt{N_{\text{overlap}}} \cdot \text{SER} \approx 836 \text{ nm}$  ( $k = 1$ ).

## 8 Conclusion

The stitching interferometry setup with absolute distance and angle measurements for freeform surfaces has been successfully tested. A spherical specimen of 50 mm in diameter and 10 m in

radius of curvature has been measured as a proof of principle. The interferometric measurement, the scanning measurement with a chromatic confocal sensor and the manufacturers' specifications agree well for the radius of curvature. An uncertainty budget has been set up for the sub-aperture stitching interferometry measurement. The most important contributions to the uncertainty budget are the lateral errors due to the stages' straightness, the angle measurements and the residuals from the stitching. The interferometry itself is less critical than the mechanical components of the setup. The radius of curvature determined for the topography is very sensitive to height errors, as the diameter of the spherical specimen is small compared to the radius of curvature.

The measurement of the car's side window showed good agreement with a profile measurement taken using a chromatic confocal sensor with an RMS difference of 370 nm over 170 mm in length. The topography uncertainty for this specimen is dominated by the residuals from the stitching. The residuals mainly result from systematic angle and position errors. The accuracy can be improved by calibrating the rotation encoders with an external high-accuracy angle measurement device. For a larger specimen, the change of the direction of gravity for the tiltmeters has to be corrected.

PTB is currently developing a new traceable form measurement system for large optics up to 1.5 m in diameter.<sup>27</sup> Methods and experiences gained while working on this publication will be used in the new system.

## Acknowledgments

The authors declare no conflicts of interest.

## References

1. P. Murphy et al., "Stitching interferometry: a flexible solution for surface metrology," *Opt. Photonics News* **14**, 38–43 (2003).
2. L. L. Deck and P. J. de Groot, "The state of the art in swept-wavelength laser Fizeau interferometry," *Proc. SPIE* **11817**, 118170N (2021).
3. J. P. Rolland et al., "Freeform optics for imaging," *Optica* **8**, 161–176 (2021).
4. D. Golini, G. Forbes, and P. Murphy, "Method for self-calibrated sub-aperture stitching for surface figure measurement," US Patent 6,956,657 (2005).
5. Y. B. Seo et al., "Subaperture stitching wavelength scanning interferometry for 3D surface measurement of complex-shaped optics," *Meas. Sci. Technol.* **32**, 045201 (2021).
6. C. M. Supranowitz et al., "Enhanced resolution and accuracy of freeform metrology through subaperture stitching interferometry," *Proc. SPIE* **10448**, 1044818 (2017).
7. V. Heikkinen et al., "Multi-sensor optical profilometer for measurement of large freeforms at nm-level uncertainty," *Surf. Topogr.: Metrol. Prop.* **8**, 045030 (2020).
8. T. Dresel et al., "Advances in flexible precision aspheric form measurement using axially scanned interferometry," *Proc. SPIE* **11889**, 1188905 (2021).
9. C. Zhao, "Computer-generated hologram for optical testing: a review," *Proc. SPIE* **11813**, 118130K (2021).
10. E. Garbusi, C. Pruss, and W. Osten, "Interferometer for precise and flexible asphere testing," *Opt. Lett.* **33**, 2973–2975 (2008).
11. I. Fortmeier et al., "Round robin comparison study on the form measurement of optical freeform surfaces," *J. Eur. Opt. Soc.-Rapid Publ.* **16**(1), 2 (2020).
12. A. Vivo, R. Barrett, and F. Perrin, "Stitching techniques for measuring x-ray synchrotron mirror topography," *Rev. Sci. Instrum.* **90**(2), 021710 (2019).
13. L. Huang et al., "Two-dimensional stitching interferometry based on tilt measurement," *Opt. Express* **26**, 23278–23286 (2018).
14. M. Schulz et al., "Traceable multiple sensor system for absolute form measurement," *Proc. SPIE* **5878**, 58780A (2005).
15. P. Su et al., "Software configurable optical test system: a computerized reverse Hartmann test," *Appl. Opt.* **49**, 4404–4412 (2010).

16. A. V. Maldonado, P. Su, and J. H. Burge, "Development of a portable deflectometry system for high spatial resolution surface measurements," *Appl. Opt.* **53**, 4023–4032 (2014).
17. G. Ehret et al., "Deflectometric systems for absolute flatness measurements at PTB," *Meas. Sci. Technol.* **23**, 094007 (2012).
18. R. Henselmans et al., "The nanomefos non-contact measurement machine for freeform optics," *Precis. Eng.* **35**(4), 607–624 (2011).
19. G. Berger and J. Petter, "Non-contact metrology of aspheric surfaces based on MWLI technology," *Proc. SPIE* **8884**, 88840V (2013).
20. H. Tsutsumi, K. Yoshizumi, and H. Takeuchi, "Ultraprecisely accurate 3D profilometer," *Proc. SPIE* **5638**, 387–394 (2005).
21. M. A. Herráez et al., "Fast two-dimensional phase-unwrapping algorithm based on sorting by reliability following a noncontinuous path," *Appl. Opt.* **41**, 7437–7444 (2002).
22. H. Kikuta, K. Iwata, and R. Nagata, "Absolute distance measurement by wavelength shift interferometry with a laser diode: some systematic error sources," *Appl. Opt.* **26**, 1654–1660 (1987).
23. H. Shahinian, C. D. Hovis, and C. J. Evans, "Effect of retrace error on stitching coherent scanning interferometry measurements of freeform optics," *Opt. Express* **29**, 28562 (2021).
24. J. A. Stone et al., "Advice from the CCL on the use of unstabilized lasers as standards of wavelength: the helium–neon laser at 633 nm," *Metrologia* **46**, 11–18 (2008).
25. U. Griesmann, "Three-flat test solutions based on simple mirror symmetry," *Appl. Opt.* **45**, 5856 (2006).
26. R. D. Geckeler et al., "New frontiers in angle metrology at the PTB," *Measurement* **73**, 231–238 (2015).
27. G. Ehret, J. Spichtinger, and M. Schulz, "Status of highly accurate flatness metrology at PTB for optics up to 1.5 meters in diameter," *Proc. SPIE* **11899**, 118991E (2021).

**Jan Spichtinger** is a PhD student at the Physikalisch-Technische Bundesanstalt, Braunschweig. He received his BS and MS degrees in physics from Heidelberg University in 2015 and 2018. His current research interests include optical form metrology and interferometry.

**Michael Schulz** was awarded his German diploma degree in physics in 1983, and his PhD in natural sciences from the University of Paderborn, Germany, in 1988. Since 1990, he has been working in the field of highly accurate optical form measurement techniques. He is the head of the Form and Wavefront Metrology-Working Group of the Physikalisch-Technische Bundesanstalt, the National Institute of Science and Metrology of Germany. He is the author of more than 150 papers.

**Gerd Ehret** received his doctorate degree (Dr.-Ing.) from the University of Hanover in 2003. He is head of the PTB department "Image and Wave Optics" and head of the PTB working group "Flatness Metrology." His working group develops interferometric and deflectometric-based flatness metrology. He has more than 20 years of experience in optical metrology (optical flatness/form metrology, optical microscopy, optical modeling, and shearing technology) and has published more than 100 scientific papers in this field.

**Rainer Tutsch** received a doctorate degree (Dr.-Ing.) from RWTH Aachen for a scientific thesis on the measurement of aspheric optical elements. From 1995 till 2000, he worked as the head of R&D for a German company. Since 2000, he has been the head of the Institute of Production Metrology at Braunschweig University.